

Notice of Copyright:

This manuscript has been co-authored by UT-Battelle, LLC, under contract DE-AC05-00OR22725 with the US Department of Energy (DOE). The US government retains and the publisher, by accepting the article for publication, acknowledges that the US government retains a nonexclusive, paid-up, irrevocable, worldwide license to publish or reproduce the published form of this manuscript, or allow others to do so, for US government purposes. DOE will provide public access to these results of federally sponsored research in accordance with the DOE Public Access Plan (<http://energy.gov/downloads/doe-public-access-plan>).

# Accelerating Neutron Scattering Data Collection and Experiments Using AI Deep Super-Resolution Learning

Ming-Ching Chang<sup>1</sup>, Yi Wei<sup>1</sup>, Wei-Ren Chen<sup>2</sup>, Changwoo Do<sup>2†</sup>

<sup>1</sup>University at Albany, State University of New York, NY, USA.

<sup>2</sup>Neutron Scattering Division, Oak Ridge National Laboratory, Oak Ridge, USA.

**Synopsis** Pursuing hardware upgrades to provide brighter beams for material studies has been the paramount goal of every neutron scattering facility. In this report we demonstrate an alternative route to circumvent the limitation of neutron flux: Using recent advancements in artificial intelligence (AI), namely image super-resolution deep convolutional neural network (CNN), we demonstrate feasibility of accelerating data collection of coherent small angle neutron scattering intensities by increasing detector binning size and subsequently recovering high-resolution images via trained CNN models.

**Abstract** We present a novel methodology of augmenting the scattering data measured by small angle neutron scattering via an emerging deep convolutional neural network (CNN) that is widely used in artificial intelligence (AI). Data collection time is reduced by increasing the size of binning of the detector pixels at the sacrifice of resolution. High-resolution scattering data is then reconstructed by using AI deep super-resolution learning method. This technique can not only improve the productivity of neutron scattering instruments by speeding up the experimental workflow but also enable capturing kinetic changes and transient phenomenon of materials that are currently inaccessible by existing neutron scattering techniques.

**Keywords:** **neutron scattering, super-resolution, convolutional neural network, deep learning, artificial intelligence**

## 1. Introduction

It is now a common practice of using neutron scattering techniques to investigate atomic-scale structure and dynamics. They possess unique advantages over other scattering techniques such as x-ray or light, with the exceptional penetration power, free from radiation damage, and the ability to selectively highlight specific parts of materials via isotope labelling [1,2]. However, because the flux of neutrons is generally more than 10 orders of magnitude lower than the flux of the photons at modern light sources, long data collection time (~tens of minutes to tens of hours) is often required to achieve high-quality statistics. Therefore, making decisions on which sample to measure becomes critical component in the experimental workflow. Early decision making can optimize effective use of limited beamtime and increase science productivity. The requirement of relatively long measurement time has also limited neutrons from contributing to some of the most interesting sciences in materials research. For example, understanding dynamic response under external stimuli has been an active research field

of non-equilibrium materials [3,4]. While time-synchronised sample environment in combination with event-based processing of neutron data has enabled observation of fast dynamic changes even with neutrons [5], irreversible phenomena can still be measured only with high enough flux. Therefore, minutes to tens of seconds of time resolution has been the best time resolution which can provide good signals for studying irreversible process using neutron scatterings [6–8]. This is at least one or two orders of magnitude slower time resolution that x-ray scattering can achieve [7–9]. Considering the unique capabilities that neutrons have, enabling fast data collection using neutrons will bring new science opportunities in materials research.

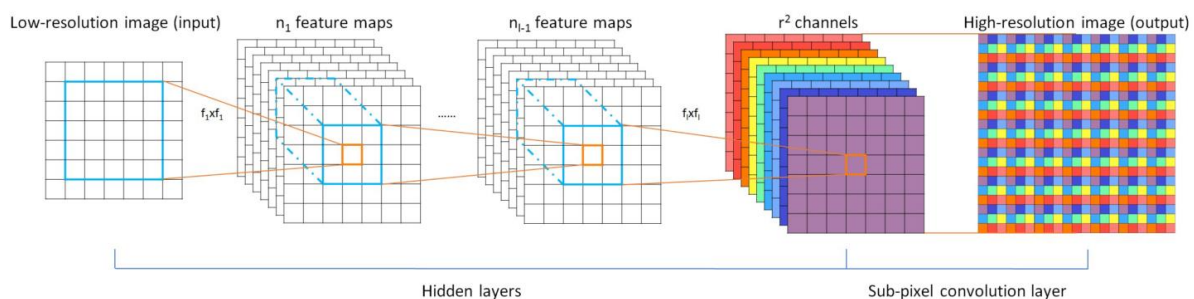
Hardware investment (constructing a bigger accelerator and/or using a brighter source) to solve these aforementioned problems is impractical, as the return on investment is not cost effective. The spallation source has begun to reach its attainable flux limit and there are still various challenges left for the new type of neutron production such as an inertial fusion method becomes realized [10]. A critical question to circumvent this limitation is whether one can reliably predict how materials scatter without having to expose samples to much brighter beams to obtain satisfactory counting statistics with reasonable measuring time. One solution is to apply data-driven machine learning methods to enhance low-resolution images or signals by learning from training samples [11,12]. Because low-resolution images can be measured much faster by binning multiple detector pixels, data collection can be effectively accelerated in this approach. The sacrificed image resolution will be recovered by the machine learning methods. Recently, due to the booming popularity of Deep Learning and in Artificial Intelligence [13], Deep Neural Networks (DNN) based methods can achieve excellent performance in many research fields including image analysis, healthcare, and natural language processing. Specific to our problem here, deep Convolutional Neural Network (CNN) based image super-resolution methods have shown promising results in enhancing low-resolution or noisy images by learning from sufficiently large training examples [14]. We see a great potential of applying the deep learning image super-resolution approach to accelerate neutron scattering data collection, particularly small angle neutron scattering data to begin with, by taking advantage of large data sets available at Spallation Neutron Source (SNS, Oak Ridge).

Image super-resolution is an active research topic in digital image processing and computer vision [15], where mostly nature (electro-optical) images are studied. Here we adopt the state-of-the-art super-resolution algorithm to neutron scattering data. The aim is to recover a high-resolution neutron scattering signal from the input low-resolution signal. Due to physical acquisition limitations in image formation, high-resolution images are in general harder (or require longer time) to capture. Thus, super-resolution technique can be applied to improve the efficiency in the acquisition of high-resolution information from merely the observed low-resolution signals. Super-resolution is an ill-posed problem, since a single pixel in low resolution image could map to multiple pixels in its high-resolution counterparts. A key assumption of many super-resolution techniques is that the high frequency pattern

is redundant and can be easily reconstructed from low frequency components. Existing super-resolution methods can be organized into three categories: (i) edge-based methods, (ii) image statistical methods, and (iii) example patch-based methods. Refer to [15] for a thorough review. Example patch-based methods have achieved good performance in traditional methods [16–19]. Sparse dictionary learning (or sparse coding) is widely used in these methods, which assumes that the image signal can be represented by a dictionary of representation atoms. This way, the redundant patterns of high-frequency signals can be represented by dictionary atoms, and the correspondence between low-resolution and high-resolution representations is learnt through the sparsity-based formulation [16,17].

How to learn a good representation for image patterns is the key point to improve the performance of super-resolution methods. DNN have shown great promise in image feature learning [20] with a large amount of training data and nonlinear transformation. DNN models are known to be capable for learning superior features that can improve the reconstruction accuracy in super-resolution. Several deep neural networks based super-resolution methods [14,21,22] with end-to-end learning have shown superior performance than the traditional sparse coding methods based on hand-crafted features. The basic idea of these methods is to learn a good feature representation in the top several layers of neural networks and map the low-level feature to high-resolution signal space. The whole process is trained end-to-end with little pre/post-processing beyond the optimization.

In this work, we apply the super-resolution convolutional neural network of [14] to predict high-resolution scattering images from the low-resolution scattering inputs. By grouping detector pixels, good statistics data can be obtained at much faster rate. Therefore, successful super-resolution method can effectively accelerate the experimental time. A reasonably trained super-resolution neural network is demonstrated by using randomly selected large neutron data sets under identical instrument configuration from the Extended Q-range Small Angle Neutron Scattering instrument (EQ-SANS) at SNS.



**Figure 1** Architecture of the efficient sub-pixel convolutional neural network (ESPCN) [14]. Figure adapted from [14]. The top two convolution layers extracts feature maps, while the last sub-pixel convolution layer aggregates the feature maps from low-resolution space to build the super-resolution image.

## 2. Methods

### 2.1. Data preparation

We prepare the SANS data collected from EQ-SANS at SNS to train a deep image super-resolution neural network. As of August 2018, EQ-SANS has collected more than 80,000 measurements including both transmission and scattering data at various configurations. Each instrument configuration such as sample to detector distance, choices of beam slits, sample apertures, and wavelength bands introduce unique resolution function and  $q$ -ranges, where the wavevector  $q$  is defined as  $q = 4\pi \sin(\theta) / \lambda$  with scattering angle  $\theta$  and wavelength  $\lambda$ . These are critical parameters that determines the broadening of scattering peaks and typically observed scattering patterns. For reasonable trainings, pairs of scattering images both at low-resolution and high-resolution are required. In order to isolate the effect of noise in the data, scattering images that have more than 5 million total neutron counts are preselected. Data sets are further filtered by the most widely used instrument configuration, which is 4m sample-to-detector distance and a wavelength band with 2.5Å as a minimum wavelength. As a result, total 5,573 scattering data have been selected and reduced in two resolutions (120x120 and 30x30) following standard SANS data reduction procedure using MantidPlot described elsewhere [23]. During the process of the data, material and science-specific data were all removed from the metadata. Resulting three column data (intensity,  $q_x$ ,  $q_y$ ) have been converted into 2-D array, where the value of each element is the scattering intensity at the position of  $q_x$  and  $q_y$ . We filled the element with 0 if the value of that position is missing.

### 2.2. Pre-processing

Since the input data is of large range ( $0 < \text{intensity} < \sim 51,000$ ), training neural networks with original range will cause the backpropagation optimization method hard to converge. We applied normalization method () on data to rescale it to a smaller range.

$$x' = \ln(x + \varepsilon)$$

where  $\varepsilon$  is set to make the base positive, we use 3 in our experiment. After rescaling, the range of input is (0, 16).

### 2.3. Neural Network Model

In this work, we adopt the efficient sub-pixel convolutional neural network (ESPCN) [14] for our experiment due to its good performance and time-efficiency. The ESPCN takes a low-resolution (LR) image (signal)  $I^{LR}$  with tensor size  $H \times W \times C$  as input where  $C$  is the colour channel, and try to estimate the high-resolution (HR) ground truth  $I^{HR}$  with a specified upscaling ratio  $r$ . We denote the output of the neural network as  $I^{SR}$ , which has the same tensor size with  $I^{HR}$  as  $rH \times rW \times C$ . The architecture of ESPCN is shown in **Fig. 1**, it consists of two parts: the first  $l$  convolutional layers are

applied to  $I^{LR}$  to learn the feature representation of input signal, then a sub-pixel convolution layer upscales the low-resolution feature maps to produce  $I^{SR}$ .

The first  $L - 1$  convolutional layers can be represented as follows:

$$f^1(I^{LR}; W_1, b_1) = \phi(W_1 * I^{LR} + b_1)$$

$$f^l(I^{LR}; W_{1:l}, b_{1:l}) = \phi(W_l * f^{l-1}(I^{LR}) + b_l)$$

Where  $W_l, b_l$  are learnable network weights and bias for each convolutional layer.  $\phi(\cdot)$  is the activation function. The Rectified Linear Unit (ReLU) used in the network as activation function is:

$$\text{ReLU}(x) = \max(0, x)$$

After the first  $L - 1$  convolutional layers,  $I^{LR}$  is represented by a  $H \times W \times r^2 C$  tensor. To generate the desired high-resolution image  $I^{SR}$  from LR feature maps, a sub-pixel convolution layer is used of a deconvolutional layer as in [24]. Both proposed sub-pixel convolution layer and deconvolutional layer can map the same feature maps in LR space to HR space, however the sub-pixel convolution layer contains more parameters in convolution filters, thus with more representation capability in upsampling the input signal with the same computational speed. The last sub-pixel convolution layer is:

$$I^{SR} = f^L(I^{LR}) = PS(W_L * f^{L-1}(I^{LR}) + b_L)$$

where  $PS$  is a periodic shuffling operator that rearranges the elements of a  $H \times W \times r^2 C$  tensor to a tensor with shape  $rH \times rW \times C$  which is the estimated super-resolution image  $I^{SR}$ . Detailed implementation can be found in [14,25]. To train the parameters of network, a pixel-wise mean squared error (MSE) loss is applied as the objective function to measure the reconstruction errors:

$$l(W_{1:L}, b_{1:L}) = \frac{1}{r^2 HW} \sum_{i=1}^{rH} \sum_{j=1}^{rW} (I_{i,j}^{HR} - f_{i,j}^L(I^{LR}))^2$$

## 2.4. Training setting

For the ESPCN, we followed the default setting of neural networks in [14] and set upscale factor  $r = 3$ . The take 70% of data samples for training and the remaining 30% samples for testing. The learning rate is set to 0.001. The training loss is converged after 2000 epochs. The training process takes roughly three hours on a NVIDIA TITAN X GPU on 3,800 training samples.

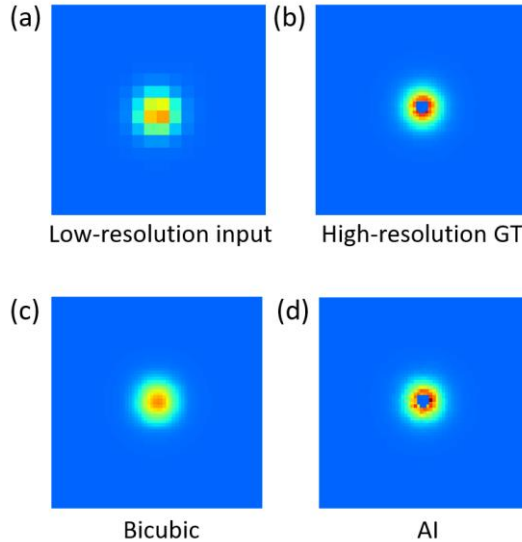


**Figure 2** Example of super-resolution prediction on SANS data. (a) Low-resolution input. (b) high-resolution ground truth (GT). (c) high-resolution image predicted by bicubic algorithm. (d) high-resolution image predicted by AI model trained using EQ-SANS data. Comparison shows that the AI-predicted image shows better agreement with the high-resolution GT including the reproduction of the beamstop feature. Cropped 15×15 and 60×60 pixels around the centers of the full images are shown to help visual comparison.

### 3. Results

**Fig. 2** shows an example super-resolution result in comparison with the baseline bicubic upsampling applied to the raw SANS data. The input image is in the resolution of 30 by 30 pixels. High resolution prediction is 120 by 120, which is 16 times more pixels. The scattering image shown here exhibits one of the commonly observed scattering characteristics of SANS data. The scattering intensity is strongest at the lowest  $q$  value and decays as the  $q$  increases. Both bicubic algorithm and the proposed AI super-resolution method successfully predict the decaying intensity as a function of  $q$  qualitatively well. However, noted that the AI predicted image not only produced the scattering intensity profile but also produced one of the instrument feature, a beamstop. In SANS experiments, beamstop is often used to block direct beam of neutrons. The beamstop absorbs neutrons, therefore it appears as empty pixels. At EQ-SANS, 60 mm diameter beamstop is used for 4m sample to detector distance configuration. Considering that the detector size is about 1m×1m, the pixel size of the low resolution image is estimated to be around ~33mm. Therefore, the beamstop is not apparent in the low resolution image due to the strong low- $q$  scatterings smearing from the nearby pixels in **Fig. 2**. Since there is no clear evidence of empty pixels representing a beamstop, bicubic algorithm fills the center pixels with predicted intensity. However, trained AI has identified the beamstop as one of the instrument feature and predicted positions of the empty pixels in the high resolution output even when the beamstop is not visually identified in the low resolution input. As a result, the difference map shows strong peak at the

center of the image for the bicubic algorithm while the AI prediction shows very good agreement over all pixels. In **Fig. 3**, the 1-D averaged scattering intensities from different sources are compared. Both results from bicubic algorithm and AI prediction exhibit reasonable agreement with the groundtruth. It is mainly due to the continuous and monotonic nature of this type of scattering profile, where bicubic algorithm can perform excellent. However, it should be pointed out that the AI predicted curve showed better accuracy especially at low- $q$  ranges while the bicubic algorithm produced more deviations from the groundtruth than the AI model.

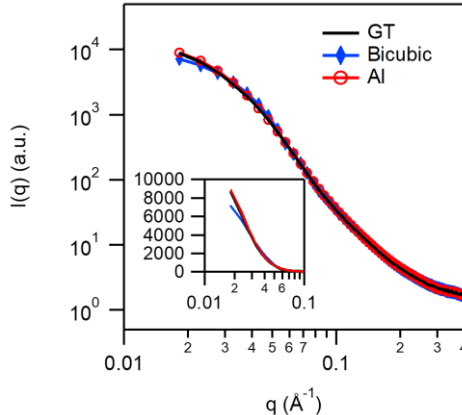


**Figure 3** Circular averaged scattering profiles of the data shown in **Fig. 2**. Inset is the scaled-up plot of the low- $q$  range with linear y-axis.

We next evaluate the obtained AI super-resolution model on another commonly encountered scattering pattern of SANS. The isotropic ring pattern is often observed from SANS measurements, indicating strong correlation at certain length scale. For examples, interacting colloidal systems exhibit correlation peak whose width and sharpness can provide critical information about the distribution of particles and characteristics of interaction potentials [26]. Randomly oriented liquid crystalline phase also produce scattering peaks which will appear as rings in two dimensional scattering pattern. The position and width of the rings can be used to extract structural dimensions and degree of order [27,28]. However, accurate values of positions and widths of such scattering peaks cannot be extracted from low resolution scattering images as shown in **Fig. 4a**. In our test, AI has shown significantly better performance in recovering peak position and peak width compared to the bicubic algorithm. Bicubic algorithm resulted in distorted ring shape in 2D with much broader peak width, which would give incorrect physical interpretation. The difference of the peak shape can be clearly observed from the 1-D averaged scattering curve in **Fig 4b**. The bicubic algorithm not only fails to predict correct width of the peak but also predicts the peak position slightly off. In contrast, AI model's prediction shows excellent agreement with the groundtruth data.

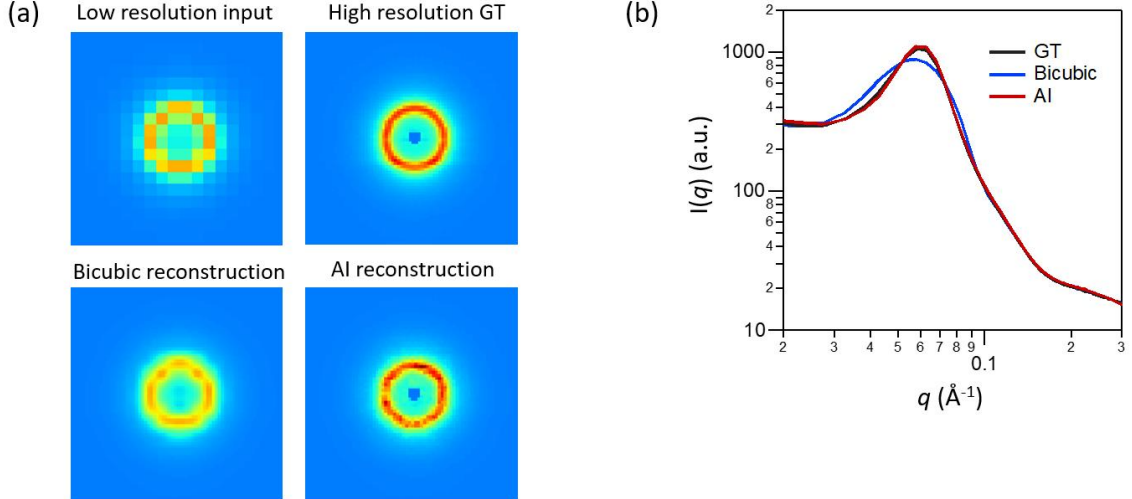


**Figure 4** (a) Example of two dimensional scattering images with an isotropic peak, demonstrating the success of AI model in predicting the instrument resolution correctly. (b) Circular averaged scattering profiles of the data shown in (a).

In SANS, anisotropic two-dimensional scattering patterns can be observed from samples that exhibit molecular level alignment and orientation. Soft materials under shear or stretching are well known examples that show such alignment, resulting in anisotropic scattering patterns [29–31]. In principle, microstructures of deformed soft materials can be studied from the anisotropic scattering patterns, which can elucidate the relation between the structural deformation and resulting physical properties. Recent theoretical and experimental studies [32,33] have also proven the importance of quantitative analysis on two dimensional scattering data for the fundamental understanding of rheological behavior.

Our AI model has shown success in predicting high-resolution scattering pattern from the low-resolution anisotropic scattering data as well. **Fig. 5** shows typical anisotropic pattern of SANS measured at low-resolution and its high-resolution counterpart along with predictions by bicubic algorithm and AI model. From the 2D pattern, both high-resolution images reconstructed by the AI and bicubic algorithm show similar anisotropy found in the groundtruth image. This again shows that the bicubic algorithm works reasonably well when the scattering profile has slow and monotonic  $q$  dependency without sharp transitions. The anisotropy represented by the integrated intensity from  $0.03 \text{\AA}^{-1} < q < 0.1 \text{\AA}^{-1}$  along the annulus also indicate the level of anisotropy is well-reproduced by both algorithms. (**Fig. 6a**) One dimensional scattering intensities from the predicted 2D patterns are also compared by taking  $\pm 10^\circ$  sectional average along the horizontal and vertical direction. While both algorithms predicted the horizontal profiles with reasonably good agreement, AI prediction showed slightly better performance in reconstructing scattering intensity along the vertical direction. Along with the previously demonstrated results, AI model proves to be more efficient and precise in predicting

scattering images with sharp transitions. It seems that the AI model was able to obtain optimized instrument resolution kernel from the randomly selected training data set. This also suggests that it is important to separate data sets with different instrument response functions for training in order to expect accurate predictions from the trained model.

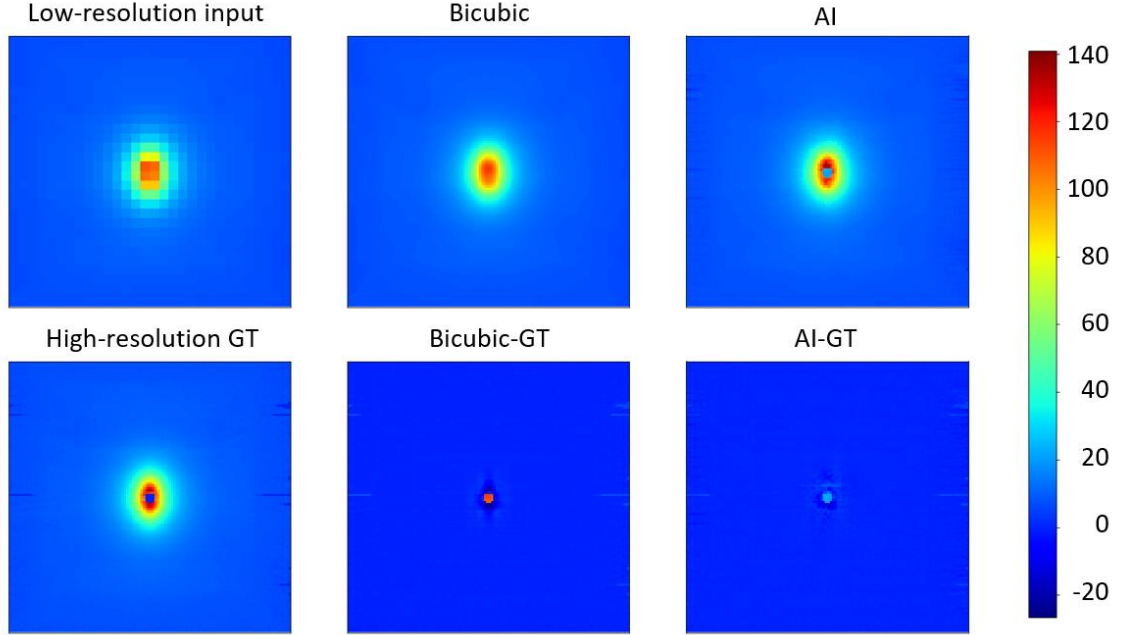


**Figure 5** Example of 2D anisotropic scattering images.

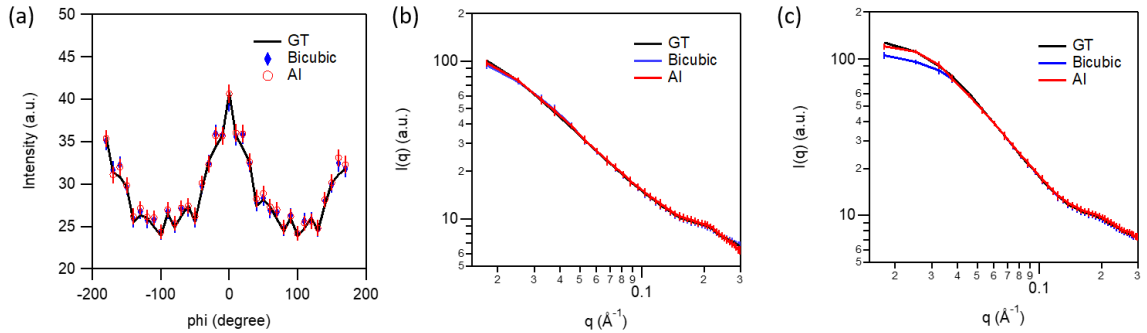


**Figure 6** (a) Annulus plot of integral intensities showing anisotropic character of the 2D data. (b) Sectional average along the horizontal direction of scattering patterns from **Fig. 5**. (c) Sectional average along the vertical direction of scattering patterns from **Fig. 5**.

In order to provide overall performance comparison between the AI model and the bicubic algorithm, differences between 1D averaged  $I_{AI}(q)$  and  $I_{GT}(q)$  have been estimated for all 1662 test cases using  $\chi^2 = \sum (I_{AI \text{ or } Bi}(q) - I_{GT}(q))^2 / N$ , where  $N$  is the number of  $q$  values used in the summation. They are summarized in **Fig. 7a**, which shows that  $\chi^2_{AI}$  are overall smaller than  $\chi^2_{Bi}$ . To a first approximation, this means that there are more cases where AI model performed better than bicubic

algorithm in reconstructing high-resolution data. However, cases with very high  $\chi^2$  values are also observed, indicating that both methods failed to achieve good agreement with ground truth. In **Fig. 7b**, only the successful cases (1420 cases out of 1662) are shown, where the smaller  $\chi^2$  of the two is less than 10, suggesting reasonably successful prediction for the high-resolution scattering images by one of the two algorithms. Red triangles indicate test cases where AI model's prediction was quantitatively better than the bicubic algorithm. And blue circle represents test cases where bicubic algorithm had smaller  $\chi^2$ . Interestingly, the distribution between red and blue data points can tell us about effectiveness of the AI model. The fact that blue data points are well concentrated in the  $\chi_{max}^2 < 10$  shows that both AI and the bicubic models in fact predicted the high-resolution images reasonably well and the difference between the predictions was small. However, when AI was more successful than bicubic algorithm, the  $\chi_{max}^2$  values extend relatively large up to  $\sim 100$ . In other words, AI's prediction made much more significant improvements over the bicubic predictions. Previously introduced examples demonstrated how AI's predictions can be effective in predicting certain features of scattering images by learning characteristics of the instrument responses.

#### 4. Conclusion

By utilizing randomly selected SANS data from an identical instrument configuration, an AI super-resolution model has been trained. Our results demonstrate that the AI model trained in this way can successfully reconstruct high-resolution scattering images from the low-resolution data. Especially, AI model learned instrument specific characteristics such as presence of the beamstop and instrument resolution. Because the AI model incorporates the instrument resolution in reconstructing high-resolution scattering images, it achieved much better quantitative agreement with the ground truth than the bicubic algorithm. Being able to use low-resolution detector images is equivalent to reducing measurement time. If successfully integrated with existing beamlines after further improvement, this will not only accelerate the scientific process as it can help scientists' early decision making (*e.g.*, to stop the current scattering experiment if something is awry), but also provide new information for time-resolved scattering experiments at timescales which has not been possible before.

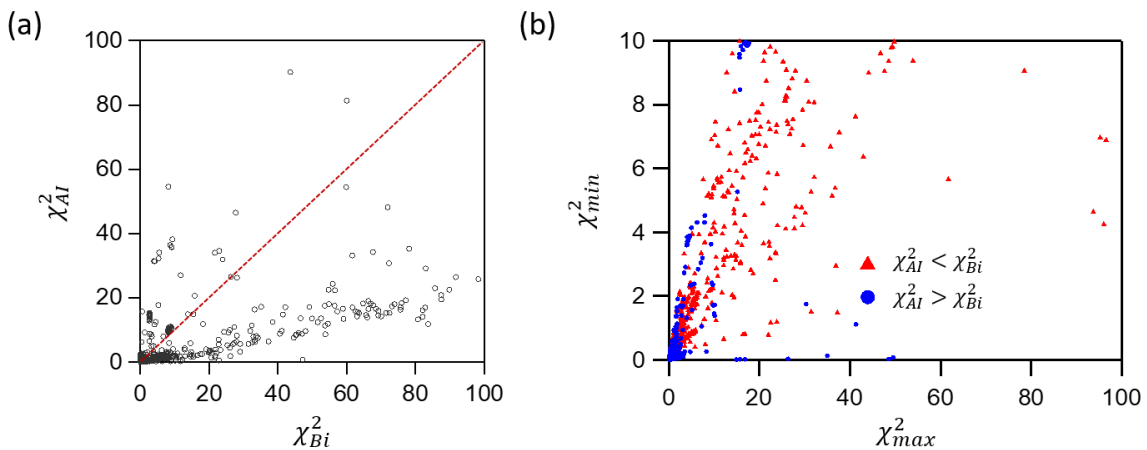


**Figure 7** . Distribution of  $\chi^2$  values for test cases with  $\chi^2_{min} < 10$ . Red triangles indicate cases where AI performed better than bicubic algorithm based on  $\chi^2$  values. Blue circles represent cases where bicubic algorithm resulted in smaller  $\chi^2$  values.

**Acknowledgements** The Research at Oak Ridge National Laboratory's Spallation Neutron Source was sponsored by the Scientific User Facilities Division, Office of Basic Energy Sciences, U.S. Department of Energy.

## References

- [1] P. Lindner and T. Zemb, editors , "Neutrons, X-Rays And Light: Scattering Methods Applied To Soft Condensed Matter," *Neutrons, X-Rays and Light: Scattering Methods Applied to Soft Condensed Matter* (North-Holland, 2002).
- [2] D. Richter, M. Monkenbusch, A. Arbe, and J. Colmenero, "Neutron Spin Echo In Polymer Systems," **174**, 1 (2005).
- [3] T. Narayanan, H. Wacklin, O. Konovalov, and R. Lund, "Recent Applications Of Synchrotron Radiation And Neutrons In The Study Of Soft Matter," *Crystallogr. Rev.* **23**, 160 (2017).
- [4] C. J. Milne, T. J. Penfold, and M. Chergui, "Recent Experimental And Theoretical Developments In Time-Resolved X-Ray Spectroscopies," *Coord. Chem. Rev.* **277–278**, 44 (2014).
- [5] G. E. Granroth, K. An, H. L. Smith, P. Whitfield, J. C. Neufeld, J. Lee, W. Zhou, V. N. Sedov, P. F. Peterson, A. Parizzi, H. Skorpenske, S. M. Hartman, A. Huq, and D. L. Abernathy, "Event-Based Processing Of Neutron Scattering Data At The Spallation Neutron Source," *J. Appl. Crystallogr.* **51**, 616 (2018).
- [6] R. Lund, L. Willner, D. Richter, H. Iatrou, N. Hadjichristidis, P. Lindner, and IUCr, "Unraveling The Equilibrium Chain Exchange Kinetics Of Polymeric Micelles Using Small-Angle Neutron Scattering – Architectural And Topological Effects," *J. Appl. Crystallogr.* **40**, s327 (2007).
- [7] L. K. Bruetzel, P. U. Walker, T. Gerling, H. Dietz, and J. Lipfert, "Time-Resolved Small-Angle X-Ray Scattering Reveals Millisecond Transitions Of A DNA Origami Switch," *Nano*

*Lett.* **18**, 2672 (2018).

[8] A. Sauter, F. Roosen-Runge, F. Zhang, G. Lotze, R. M. J. Jacobs, and F. Schreiber, "Real-Time Observation Of Nonclassical Protein Crystallization Kinetics," *J. Am. Chem. Soc.* **137**, 1485 (2015).

[9] K. Vegso, P. Siffalovic, M. Jergel, P. Nadazdy, V. Nadazdy, and E. Majkova, "Kinetics Of Polymer–Fullerene Phase Separation During Solvent Annealing Studied By Table-Top X-Ray Scattering," *ACS Appl. Mater. Interfaces* **9**, 8241 (2017).

[10] A. Taylor, M. Dunne, S. Bennington, S. Ansell, I. Gardner, P. Norreys, T. Broome, D. Findlay, and R. Nelmes, "A Route To The Brightest Possible Neutron Source?," *Science* **315**, 1092 (2007).

[11] A. Majumdar, "Real-Time Dynamic MRI Reconstruction Using Stacked Denoising Autoencoder," *ArXiv:1503.06383v1 [Cs.CV]* (2015).

[12] L. Gondara, "Medical Image Denoising Using Convolutional Denoising Autoencoders," in *2016 IEEE 16th Int. Conf. Data Min. Work.* (IEEE, 2016), pp. 241–246.

[13] Y. LeCun, Y. Bengio, and G. Hinton, "Deep Learning," *Nature* **521**, 436 (2015).

[14] W. Shi, J. Caballero, F. Huszar, J. Totz, A. P. Aitken, R. Bishop, D. Rueckert, and Z. Wang, "Real-Time Single Image And Video Super-Resolution Using An Efficient Sub-Pixel Convolutional Neural Network," in *2016 IEEE Conf. Comput. Vis. Pattern Recognit.* (IEEE, 2016), pp. 1874–1883.

[15] Z. Wang, J. Chen, and S. C. H. Hoi, "Deep Learning For Image Super-Resolution: A Survey," *ArXiv:1902.06068 [Cs.CV]* (2019).

[16] J. Yang, "Image Super-Resolution Via Sparse Representation," *IEEE Trans. Image Process.* **19**.11 (2010).

[17] W. Dong, L. Zhang, G. Shi, and X. Wu, "Image Deblurring And Super-Resolution By Adaptive Sparse Domain Selection And Adaptive Regularization," *IEEE Trans. Image Process.* **20**, 1838 (2011).

[18] Kwang In Kim and Younghee Kwon, "Single-Image Super-Resolution Using Sparse Regression And Natural Image Prior," *IEEE Trans. Pattern Anal. Mach. Intell.* **32**, 1127 (2010).

[19] J. Yang, Z. Lin, and S. Cohen, "Fast Image Super-Resolution Based On In-Place Example Regression," in *2013 IEEE Conf. Comput. Vis. Pattern Recognit.* (IEEE, 2013), pp. 1059–1066.

[20] A. Krizhevsky, I. Sutskever, and G. E. Hinton, "ImageNet Classification With Deep Convolutional Neural Networks," in *Adv. Neural Inf. Process. Syst.* (2012), pp. 1097–1105.

[21] Y. Chen and T. Pock, "Trainable Nonlinear Reaction Diffusion: A Flexible Framework For Fast And Effective Image Restoration," *IEEE Trans. Pattern Anal. Mach. Intell.* **39**, 1256 (2017).

[22] C. Dong, C. C. Loy, K. He, and X. Tang, "Image Super-Resolution Using Deep Convolutional Networks," *IEEE Trans. Pattern Anal. Mach. Intell.* **38**, 295 (2016).

[23] W. T. Heller, M. Cuneo, L. Debeer-Schmitt, C. Do, L. He, L. Heroux, K. Littrell, S. V. Pingali, S. Qian, C. Stanley, V. S. Urban, B. Wu, W. Bras, and IUCr, "The Suite Of Small-Angle Neutron Scattering Instruments At Oak Ridge National Laboratory," *J. Appl. Crystallogr.* **51**, 242 (2018).

[24] E. Shelhamer, J. Long, and T. Darrell, "Fully Convolutional Networks For Semantic Segmentation," *IEEE Trans. Pattern Anal. Mach. Intell.* **39**, 640 (2017).

[25] W. Shi, J. Caballero, L. Theis, F. Huszar, A. Aitken, C. Ledig, and Z. Wang, "Is The Deconvolution Layer The Same As A Convolutional Layer?," *ArXiv:1609.07009 [Cs.CV]* (2016).

- [26] S.-H. Chen, J. S. Huang, and P. Tartaglia, "Structure And Dynamics Of Strongly Interacting Colloids And Supramolecular Aggregates In Solution," *Structure and Dynamics of Strongly Interacting Colloids and Supramolecular Aggregates in Solution* (Springer Netherlands, Dordrecht, 1992).
- [27] F. Castro-Roman, L. Porcar, G. Porte, and C. Ligoure, "Quantitative Analysis Of Lyotropic Lamellar Phases SANS Patterns In Powder Oriented Samples," *Eur. Phys. J. E* **18**, 259 (2005).
- [28] C. Doe, H.-S. Jang, S. R. Kline, and S.-M. Choi, "Subdomain Structures Of Lamellar And Reverse Hexagonal Pluronic Ternary Systems Investigated By Small Angle Neutron Scattering," *Macromolecules* **42**, 2645 (2009).
- [29] Z. Wang, T. Iwashita, L. Porcar, Y. Wang, Y. Liu, L. E. Sanchez-Diaz, B. Wu, T. Egami, and W.-R. Chen, "Dynamically Correlated Region In Sheared Colloidal Glasses Revealed By Neutron Scattering," (2017).
- [30] C. R. López-Barrón, Y. Zeng, J. J. Schaefer, A. P. R. Eberle, T. P. Lodge, and F. S. Bates, "Molecular Alignment In Polyethylene During Cold Drawing Using In-Situ SANS And Raman Spectroscopy," *Macromolecules* **50**, 3627 (2017).
- [31] K. Mortensen, "Structural Studies Of Aqueous Solutions Of PEO - PPO - PEO Triblock Copolymers, Their Micellar Aggregates And Mesophases; A Small-Angle Neutron Scattering Study," *J. Phys. Condens. Matter* **8**, A103 (1996).
- [32] Z. Wang, C. N. Lam, W.-R. Chen, W. Wang, J. Liu, Y. Liu, L. Porcar, C. B. Stanley, Z. Zhao, K. Hong, and Y. Wang, "Fingerprinting Molecular Relaxation In Deformed Polymers," *Phys. Rev. X* **7**, 031003 (2017).
- [33] G.-R. Huang, Y. Wang, B. Wu, Z. Wang, C. Do, G. S. Smith, W. Bras, L. Porcar, P. Falus, and W.-R. Chen, "Reconstruction Of Three-Dimensional Anisotropic Structure From Small-Angle Scattering Experiments," *Phys. Rev. E* **96**, 022612 (2017).